Determining fundamental properties from diffraction: Electric field induced strain and piezoelectric coefficient

M. Hinterstein,[1,5,*] K.-Y. Lee,[1] S. Esslinger,[2] J. Glaum,[3] A. J. Studer,[4] M. Hoffman,[5] and M. J. Hoffmann[1]

[1]*Institute for Applied Materials, Karlsruhe Institute of Technology, 76131 Karlsruhe, Germany*

[2]*Fraunhofer Institute of Ceramic Technologies and Systems, 01277 Dresden, Germany*

[3]*Material Science and Engineering, Norwegian University of Science and Technology, 7491 Trondheim, Norway*

[4]*Australian Centre for Neutron Science, ANSTO, Locked Bag 2001, Kirrawee NSW 2232, Australia*

[5]*School of Materials Science and Engineering, UNSW, Sydney NSW 2052, Australia*

(Received 19 April 2018; revised manuscript received 29 April 2019; published 17 May 2019)

Neutron powder diffraction was used *in operando* to determine the macroscopic strain and piezoelectric coefficient as a function of applied electric field in a technically relevant actuator material. We were able to individually investigate the two coexisting phases in the material and reveal the origin of maximized strain at phase boundaries. Insight into the strain mechanisms gives evidence that, on average, the classic inverse piezoelectric effect does not apply for polycrystalline materials.

DOI: 10.1103/PhysRevB.99.174107

I. INTRODUCTION

Piezoelectric ceramics exhibit the remarkable ability to couple elastic strain and polarization under the influence of an applied electric field. Among the various types of devices, actuators rely on high electric fields to generate high strains and forces. Prominent examples are multilayer stack actuators used, e.g., in inkjet printers [1] and injectors in modern combustion engines [2] to increase efficiency, as active vibration damping in trains, planes, or cars to guarantee comfortable traveling [3], and they play an important role for nanopositioning in microscopes, monochromators, or detectors [4]. For significant increases in efficiency and clock speed even a concept for nanoactuator-based post-complementary metal-oxide semiconductor digital switches has been proposed [5], which demonstrates the wide range of applications for this class of materials. Meanwhile actuators are produced in millions of pieces every year and the number is growing rapidly.

Most of these devices are based on doped lead zirconate titanate ceramics with compositions near the so-called morphotropic phase boundary (MPB) [6], which separates the tetragonal from the rhombohedral stability region and where the relevant functional properties approach their maximum. The crystal structure at the MPB is a matter of controversial debate for many years, sparked by indications of a monoclinic phase [7]. Theories range from actual monoclinic symmetry [7] over real structure effects in the stability region of nanodomains [6] to coherently diffracting nanotwin superlattices [8]. It has been shown that the complex micro- and nanodomain structures at the MPB [9] result in local structures that cannot be described with a simple average structure model [10]. Although calculations predict polarization rotation via a monoclinic phase during the application of an electric field [11,12], the actual mechanisms are still unknown and monoclinic symmetry might be a metastable intermediate step with unknown kinetics [13].

When the composition approaches the MPB, the piezoelectric properties reach a maximum and the unit-cell distortions of the neighboring phases decrease [14]. This decreases the activation energy for a field-induced phase transformation, which can then be activated by electric fields in the kV/mm range. Therefore, the most interesting compositions for applications exhibit a phase coexistence of highly correlated phases [15–17], which complicates structural analyses. However, we recently developed a comprehensive method to analyze all strain mechanisms with a **S**train, **T**exture, and **R**ietveld **A**nalysis for **P**iezoceramics (STRAP) from powder diffraction. The well-known strain mechanisms in piezoceramics are the intrinsic converse piezoelectric effect and extrinsic domain switching [18]. Furthermore, we demonstrated the importance of a field-induced phase transformation as additional strain mechanism [16,17,19–23]. When a large field-induced strain is observed, the field-induced phase transformation is reversible and stable over many cycles [15–17,20,23].

We already demonstrated that STRAP is capable of calculating the overall macroscopic response to an applied electric field based on a single structure model of coexisting phases [15,21]. Since the model yields all structural information for every phase, we show in this paper that this offers the unique possibility to investigate the *individual* contributions of *each* phase to the overall macroscopic response. STRAP allows correlation of the macroscopic behavior of large samples with the crystal structure during application of the field ("*in operando*").

Here, we present the reconstruction of the macroscopic strain hysteresis with STRAP with a structure model based on the atomic scale. The fact that STRAP delivers a full set of structural parameters gives insight into the strain mechanisms relevant during a bipolar cycle of a commercial actuator material.

*manuel.hinterstein@kit.edu

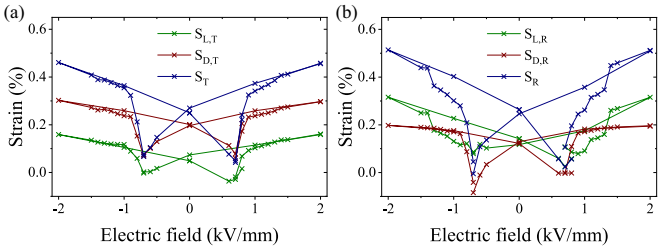

FIG. 1. Strain loops calculated from Rietveld refinement with texture analysis for (a) the tetragonal phase and (b) the rhombohedral phase. The total strain (S_T, S_R) is a phase weighted sum of the lattice strain ($S_{L,T}$, $S_{L,R}$) and the domain switching strain ($S_{D,T}$, $S_{D,R}$) of each phase.

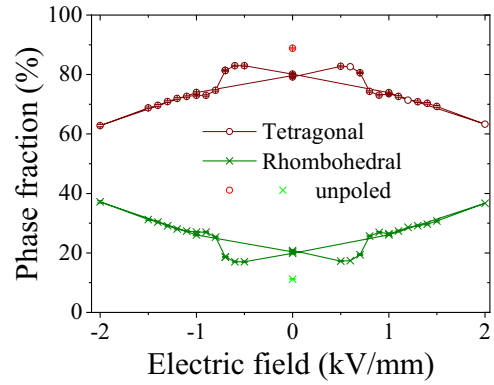

FIG. 2. Field-dependent evaluation of the phase fractions.

II. EXPERIMENTAL METHODOLOGY

Sintered ceramics of the technologically applied actuator material PIC 151($Pb_{0.99}[Zr_{0.45}Ti_{0.47}(Ni_{0.33}Sb_{0.67})_{0.08}]O_3$, PI Ceramics, Lederhose, Germany) [24] were cut and polished into rectangular bars of 3.5×3.5×25 mm. Platinum electrodes of approximately 50 nm were sputtered on two opposing long sides of the samples. Neutron-diffraction data were collected at the Wombat beamline of the Australian Nuclear Science and Technology Organization (ANSTO) in Sydney, Australia at two different wavelengths for each step during the hysteresis. A shorter wavelength of $\lambda = 1.63$ Å was used for a large-Q range and a longer wavelength of $\lambda = 2.41$ Å for high angular resolution. The electric field was applied via a TREK high-voltage amplifier in steps of 0.1 kV/mm from 0.5 to 1.5 kV/mm and in steps of 1.0 kV/mm from 2.0 to 0.0 kV/mm as described elsewhere [25]. Rietveld refinement was performed using the software package MAUD (Materials Analysis Using Diffraction) [26] with a tetragonal $P4mm$ and a rhombohedral $R3m$ phase. The exact details of the experiment and refinement of the STRAP method can be found elsewhere [15]. Direct macroscopic measurements, which were used to compare with STRAP-derived values, were taken with an aixACCT TF analyzer (TF1000, aixACCT, Germany). In continuous mode, frequencies from 10 mHz to 1 Hz were accessible. In static mode a range of field points were set for a defined period of time, giving strain loops with frequencies of 10 mHz, 555 μHz, and 16 μHz.

III. RESULTS AND DISCUSSION

The STRAP method used here quantifies three known strain mechanisms [15]. The phase fractions, which characterize the field-induced phase transformation, are extracted from a Rietveld refinement. The domain switching strain is modeled with a texture model and the lattice strain with a strain model. Since Rietveld refinement is based on a single structure model, only a single set of lattice parameters is used for each phase. The orientation-dependent change of the lattice parameters is accounted for with the strain model Weighted Strain Orientation Distribution Function (WSODF) [27].

Fig. 1 depicts the strain mechanisms for the tetragonal and the rhombohedral phase over a full bipolar cycle. Note that each point represents the results of a full STRAP refinement. Similarly to our previous results [15], the tetragonal phase exhibits a high domain switching strain $S_{D,T}$, whereas the rhombohedral phase exhibits a high lattice strain $S_{L,R}$. Thus the two phases respond differently to an applied electric field. For both phases the coercive field E_C can be clearly observed where the strain decreases to a minimum value. The diffraction-based analysis gives absolute values directly, without resorting to macroscopic measurements. Therefore, even without knowing the previous history of a sample, absolute strain values can be extracted. Additionally, the method can characterize all strain mechanisms for both contributing phases individually. For PIC151 both phases have the same coercive field of 0.7 kV/mm at this particular frequency.

For the tetragonal phase the domain switching strain $S_{D,T}$ has a significantly sharper response at the coercive field E_C than the lattice strain $S_{L,T}$. However, while the lattice strain $S_{L,T}$ is reduced to zero at E_C, the domain switching strain retains a residual value of 0.06% on the negative side and 0.07% on the positive side of the hysteresis loop. For the rhombohedral phase the responses are similar for both domain switching and lattice strain. Both strain mechanisms show no significant strain values at E_C, which results in patterns that appear as from an unpoled material.

Figure 2 shows the field-dependent evolution of the phase fractions. After poling, the tetragonal phase fraction is significantly reduced. With increasing field, the tetragonal phase fractions first increase slightly but do not reach the values for the unpoled state. Then they decrease continuously. This is in good agreement with previous observations using x rays [17,20] and neutrons [15]. The combined values of the strain mechanisms can be weighted with the phase fractions F of the tetragonal and the rhombohedral phase:

$$S = F_T(S_{L,T} + S_{D,T}) + F_R(S_{L,R} + S_{D,R}) \quad (1)$$

This combined strain S, calculated from neutron diffraction, is plotted in Fig. 3(a) together with the macroscopically measured bipolar strain loop. Since the calculations from diffraction result in absolute values for S, the macroscopically measured strain loop was shifted in S so that the remanent values match each other. Both strain loops show a similar behavior. The strain decreases at E_C for both methods to around 0.05%. However, there are significant differences for E_C and

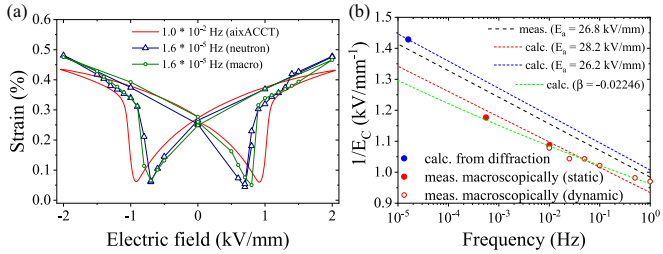

FIG. 3. (a) Bipolar strain loop macroscopically measured at 10 mHz (red), 16 μHz (green), and calculated from diffraction (blue) at an effective frequency of 16 μHz. (b) Frequency dependence of the coercive field E_C in the frequency range from 10^{-5} to 10^{0} Hz, measured macroscopically (red dots) and calculated from diffraction (blue dot). Frequency dependence of E_C fitted with different models (dashed lines) [32].

the maximum strain $S_{\max}$ at maximum electric field $E_{\max}$. This is due to the difference in measurement frequencies. While the slowest possible frequency for the aixACCT TF analyzer in continuous mode is 10 mHz with a period length of 100 s, the neutron-diffraction experiment lasted more than 17 h. This results in an effective bipolar frequency of 16 μHz, which is about three orders of magnitude slower than the macroscopic measurement. Zhou and Kamlah [28] investigated these slow kinetic effects on the strain response. The observed creep was measured directly and 600 s after field application. This translates to a rather high frequency in the mHz to Hz range and a low frequency in the μHz range. The differences in $S_{\max}$ at $E_{\max}$ due to creep were quantified to 0.05%, while E_C shifted by around 0.3 kV/mm. This correlates exactly with the shifts observed in Fig. 3(a). A specially developed slow static macroscopic measurement at 16 μHz has remarkable agreement with the calculated strain loop [Fig. 3(a), green curve].

When plotting the coercive fields as a function of frequency, the well-known logarithmic behavior can be observed [Fig. 3(b)] [29–31]. For frequencies $f \geqslant 10$ mHz the macroscopic measurements were performed continuously, while for frequencies $0.555 \leqslant f \leqslant 10$ mHz they were performed stepwise. Both measurement techniques overlap at 10 mHz and coincide perfectly. An exponential fit confirms the approximation of $E_C \propto f^{\beta}$ [31], with $\beta = -0.022$ [Fig. 3(b), green]. Comparing these results with the neutron measurements reveals a significant deviation from the logarithmic behavior, indicating additional kinetic effects at very low frequencies.

More detailed studies [32] showed that the coercive field can be expressed as

$$E_C = \frac{E_a}{-\ln(f\tau_0)}, \tag{2}$$

where E_a is the activation field, f the frequency, and τ_0 the local switching time. Zhukov *et al.* already determined the coefficients for PIC151 to $E_a = 26.8\,\mathrm{kV/mm}$ and $\tau_0 = 3.5 \times 10^{-12}$s with polarization switching experiments [32]. When plotting the frequency logarithmic against $1/E_C$, a linear dependence can be observed [29]. Assuming a constant local switching time, fits reveal an activation field strength $E_a = 28.2\,\mathrm{kV/mm}$ for the macroscopic measurements and

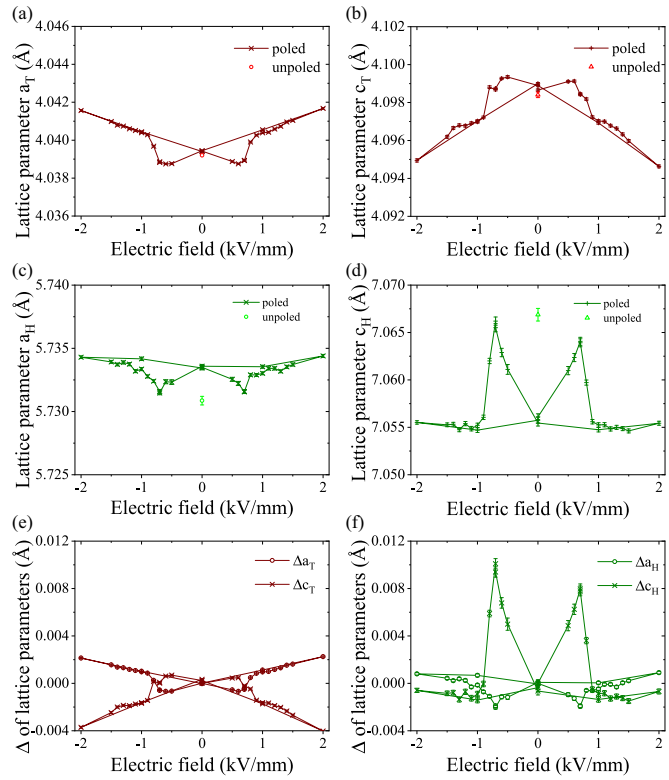

FIG. 4. Field-dependent evolution of the tetragonal (a) a_T and (b) c_T, (c) rhombohedral a_H, and (d) c_H lattice parameters in comparison with the values in the unpoled state and field-dependent change in lattice parameters for (e) the tetragonal and (f) the rhombohedral phase.

$E_a = 26.2\,\mathrm{kV/mm}$ for the neutron measurements. This indicates that for extremely low frequencies the activation field is significantly reduced. When only the macroscopic measurements are considered $E_a = 36.8\,\mathrm{kV/mm}$ and $\tau_0 = 4.6 \times 10^{-16}$s. For the complete data set $E_a = 25.3\,\mathrm{kV/mm}$ and $\tau_0 = 6.6 \times 10^{-11}$s.

The electromechanical coupling is expressed by the piezoelectric coefficient d_{33}. As Hinterstein *et al.* showed in previous work [17], d_{33} can be calculated from the change of the lattice parameters Δc and phase fractions obtained from diffraction data [Fig. 2 and Figs. 4(e) and 4(f)].

The STRAP method is based on Rietveld analysis with the program MAUD [26]. In Rietveld analysis a structure model with only a single set of lattice parameters and atomic positions is used. Therefore, the refined lattice parameters are representative for an average over the whole bulk material. Orientation-dependent differences of the lattice parameters within the material are taken into account with the WSODF model [27], incorporated in MAUD. This model accounts for the lattice strain.

Figures 4(a) and 4(b) depict the field-dependent evolution of the tetragonal and Figs. 4(c) and 4(d) of the rhombohedral lattice parameters. It becomes obvious that for the tetragonal phase the remanent values are the same as for an unpoled sample, whereas the rhombohedral values show a significant difference. Here, only at the coercive field the lattice parameters reach the same values as for an unpoled

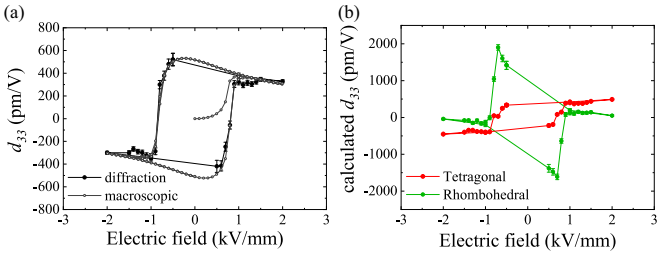

FIG. 5. Calculated $d_{33}^{¤}$ (a) as a phase-weighted sum for both phases together with the macroscopically measured d_{33}, (b) for the tetragonal and for the rhombohedral phase.

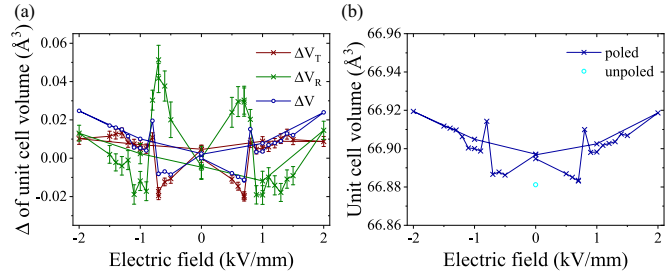

FIG. 6. (a) Field-dependent relative change in unit-cell volume for the individual phases and the phase-weighted overall volume and (b) field-dependent evolution of the combined unit-cell volume.

state. This indicates significant stresses that are induced in the rhombohedral phase during poling.

Due to the hexagonal setup of the rhombohedral phase the two sets of lattice parameters are not very well comparable. Therefore, Figs. 4(e) and 4(f) depict the relative change of the lattice parameters in comparison to the remanent value. This comparison shows the extraordinary increase of c_H at the coercive field.

The change of the lattice parameter Δc can be calculated relative to the remanent state

$$\Delta c = \frac{c^E - c^0}{c^0} \tag{3}$$

where c^0 describes the lattice parameter in the remanent state and c^E with applied electric field. Then the piezoelectric coefficient results as

$$d_{33}^{¤} = \frac{F_T}{E}.\Delta c_T + \frac{F_R}{E}.\Delta c_R \tag{4}$$

In Fig. 5 this calculated $d_{33}^{¤}$ is compared to the macroscopically measured d_{33}. Even though the calculation of the $d_{33}^{¤}$ from diffraction data is based on the simple assumption that all c axes are aligned along the electric-field vector $\boldsymbol{E}$, the agreement between the measured and calculated piezoelectric coefficient is remarkably good. The advantage of calculating the $d_{33}^{¤}$ from diffraction is that both phases are accessible individually. Figure 5(b) depicts the calculated $d_{33}^{¤}$ for the tetragonal and the rhombohedral phases. While the tetragonal $d_{33}^{¤}$exhibits the same trend as the overall d_{33} with slightly lower maximum values of around 500 pm/V, the rhombohedral $d_{33}^{¤}$ exhibits extraordinary high values around 2000 pm/V at E_C. This indicates that the high d_{33} values at phase boundaries result from the coexistence of crystallographic phases.

Since the refinements not only directly yield the strain mechanisms, but also basic attributes such as the lattice parameters (Fig. 4), the unit-cell volume V and the unit-cell distortion η of both phases can be investigated individually to understand the significant differences in electromechanical coupling of the two phases. Since PIC151 is predominantly tetragonal, the tetragonal phase also has a stronger unit-cell distortion [19].

The field-dependent phase fractions (Fig. 2) and unit-cell volumes, calculated from the lattice parameters (Fig. 4), can be used to calculate the overall unit-cell volume, depicted in Fig. 6(b). The value for the unpoled state is significantly smaller and is almost reached again at the coercive field. This evolution is a result of the stresses concluded from Figs. 4(c) and 4(d) and still follows the trend expected from a two-step 90° domain switching. Due to error propagation from the unit-cell parameters and phase fractions, the errors for the overall unit-cell volume are about one order of magnitude higher than the changes with field. Therefore, they are not shown in Fig. 6(b).

Figure 6(a) compares the relative changes in unit-cell volume for the individual phases and the overall unit-cell volume. Again, the error bars are not shown for the same reasons as mentioned for Fig. 6(b). The trends show that the tetragonal and the rhombohedral phases have exact opposite behaviors. However, due to the large tetragonal phase fraction, the tetragonal unit-cell volume dominates the overall unit-cell volume.

Figure 7(a) compares the tetragonal and the rhombohedral unit-cell distortion as a function of the electric field. When analyzing the unit-cell distortion, both phases show a pronounced response to the applied electric field [Fig. 7(a)]. For the tetragonal phase the unit-cell distortions in the unpoled and the remanent state are identical. For the rhombohedral phase the unit-cell distortion decreases significantly upon poling and stays constant over most part of the hysteresis loop with values between 0.45 and 0.50%. At E_C, η_R increases sharply to almost 0.70% on both sides of the hysteresis loop, which is in the range of the unpoled value. This coincides with the strong increase of $d_{33}^{¤}$ at E_C. Figure 7(c) displays the difference ϕ of the characteristic crystal axes [001] and [111] for both phases:

$$\phi_{001} = 1 - \frac{100_R}{001_T} \tag{5}$$

and

$$\phi_{111} = 1 - \frac{111_T}{111_R}. \tag{6}$$

The general appearance of ϕ is similar to the one of η, especially for the rhombohedral phase. According to Eq. (6) ϕ_{111} describes the expansion of the rhombohedral polar axis [111] when a tetragonal grain transforms to a rhombohedral one. For the rhombohedral phase there is a strong increase at E_C, which explains the extraordinarily high $d_{33}^{¤}$. This indicates that the extraordinarily high $d_{33}^{¤}$ is a result of the field-induced phase transformation.

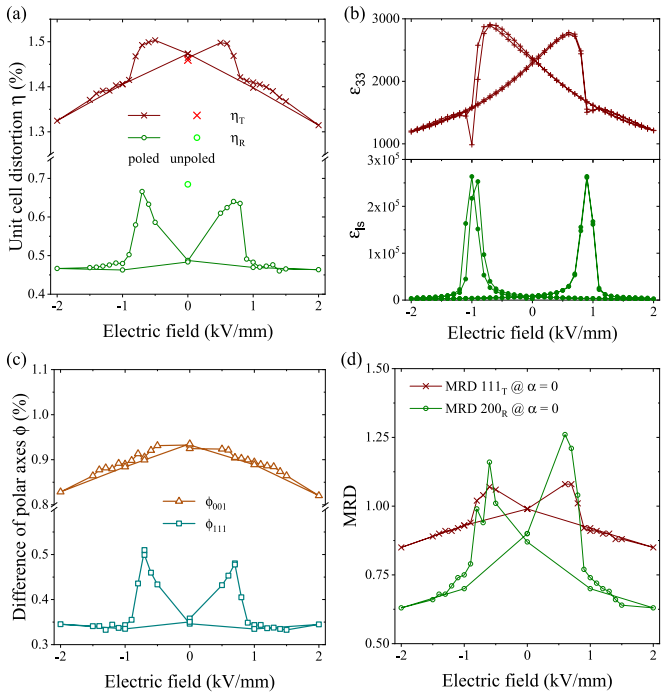

FIG. 7. (a) Unit-cell distortion for the tetragonal (η_T) and rhombohedral phase (η_R) during bipolar cycling and for comparison the unpoled values. (b) Dielectric coefficient during cycling measured macroscopically with small signal (ε_{33}) and large signal (ε_{ls}). (c) Difference of polar axes ϕ_{001} and ϕ_{111} between the tetragonal and the rhombohedral phase. (d) Pole figure density at $\propto = 0^\circ$ (along **E**) for the tetragonal 111_T and rhombohedral 200_R reflection.

For the tetragonal phase, η_T also exhibits an unexpected behavior. The classical theory of the inverse piezoelectric effect postulates an increase of $[001]_T$ and a decrease of $[100]_T$ with applied electric field, leading to an increase of η_T. The observations, however, show the exact opposite. Starting from the remanent state, η_T first increases with electric field until E_C. From there η_T constantly decreases until the maximum field.

The initial increase of η_T coincides with a macroscopic compression as observed in Fig. 3(a) at E_C. The sharp minima at E_C in Fig. 3(a) correspond to the onset of 180° domain switching. Daniels *et al.* recently showed with time-resolved high-energy -ray diffraction that 180° domain switching actually occurs via two distinct and sequential 90° domain reorientation steps [33]. When S decreases, starting from the remanent strain, and a constant volume is assumed, the sample will expand in the plane perpendicular to $\boldsymbol{E}$. When a domain is first aligned along the positive field direction and switches by 90°, it will be aligned perpendicular to $\boldsymbol{E}$ and this results in a shrinkage along $\boldsymbol{E}$. At the same time, η_T increases. This indicates that towards E_C the inverse piezoelectric effect predominates the unit-cell distortion for low electric fields. Additionally, during the two-step 90° polarization reversal, c_T can reach higher values due to reduced intergranular constraints. Together, this results in a general increase of η_T towards E_C.

The continuous decrease of η_T for higher fields can be explained due to the large tetragonal unit-cell distortion of around 1.4%. For grains with [001] aligned perpendicular to $\boldsymbol{E}$, tetragonal 90° domain switching results in a strain comparable to η_T. This would be three times higher than the macroscopically observed total strain amplitude and almost ten times higher than the unipolar strain. Due to intergranular stress constraints the maximum elongation of a grain is limited in a sintered body [18]. With increasing electric field more and more grains switch towards $\boldsymbol{E}$ depending on their orientation [34]. Therefore, the resulting η_T at high electric fields is lower than in the remanent or unpoled state. Since η_R is in the range of the maximum macroscopic strain amplitude, this behavior is not observed for the rhombohedral phase in this material.

The difference of a rhombohedral $[100]_R$ and a tetragonal $[001]_T$ axis ϕ_{001} [see Eq. (5)] for field-induced phase transformations to the tetragonal phase shows an inverted electrostrictive behavior. Again, intergranular stress constraints limit the maximum unit-cell distortion. Similarly to the case of η, ϕ_{001} is larger than ϕ_{111}. Again, these values correspond to an average from the Rietveld refinement. The lattice strain results in an orientation-dependent deviation from this mean value. Since $S_{L,R}$ is generally larger than $S_{L,T}$ for PIC151 the actual differences of the [111] and [001] axes along $\boldsymbol{E}$ are smaller for ϕ_{001} [see Eq. (5)] and larger for ϕ_{111} [see Eq. (6)] than shown in Fig. 7(c).

When comparing the values of Figs. 7(a), 7(c), and 7(d) with the macroscopically measured small signal permittivity ε_{33} and large signal permittivity ε_{ls} in Fig. 7(b), obvious similarities of the curves can be observed. Since ε_{33} results from reversible processes such as domain-wall vibrations and the inverse piezoelectric effect and ε_{ls} from both reversible as well as irreversible processes such as domain-wall motions [35], this indicates fundamentally different behaviors of the two phases.

Figure 7(d) displays the pole figure densities in multiples of random distribution of the tetragonal 111_T and rhombohedral 200_R reflections in the direction along $\boldsymbol{E}$. In both symmetries these reflections are not split and, therefore, cannot be textured in a single phase material. However, both reflections show significant texturing as a function of applied electric field and the plots show similar behavior as for the unit-cell distortions in Fig. 7(a). Both pole figure densities directly prove the orientation-dependent phase transformation. Details about this mechanism have been described elsewhere [15]. The phase transformation occurs simultaneously in both directions and is almost fully reversible, which is reflected by the values close to unity in the remanent state.

IV. SUMMARY

The results presented here provide insight into the strain mechanisms of actuator materials in detail. STRAP is able to perfectly reproduce the macroscopic strain from a crystallographic model based on the atomic scale. Since the most extreme material properties are reached in the vicinity of phase boundaries, the structure model requires and utilizes two phases. STRAP is currently the only way to analyze these coexisting phases individually. We could resolve the crystallographic behavior of both phases during bipolar cycling and show that on average the classic model of the inverse piezoelectric effect does not apply. The bidirectional

phase transformation leads to enormous values of d_{33} for the minority phase, which explains the high properties at the MPB. Therefore, the STRAP method is of great interest to the research community in the field of functional materials, especially when external stimuli are involved.

ACKNOWLEDGMENTS

This work was supported by the Deutsche Forschungsgemeinschaft (DFG) (Grant No. HI 1867/1–1). Access to use the Wombat beamline at ANSTO in Sydney, Australia through a program proposal is greatly appreciated.

[1] H.-C. Wu, T.-R. Shan, W.-S. Hwang, and H.-J. Lin, Mater. Trans. **45**, 1794 (2004).

[2] C. A. Randall, A. Kelnberger, G. Y. Yang, R. E. Eitel, and T. R. Shrout, J. Electroceram. **14**, 177 (2005).

[3] J. Lee, J. Kim, and C. C. Cheong, J. Mater. Sci. Technol. **13**, 451 (1999).

[4] A. Horst, A. Berghaeuser, M. Hinterstein, and M. Knapp, DE102012220124-B3 (2 October 2013).

[5] D. M. Newns, B. G. Elmegreen, X.-H. Liu, and G. J. Martyna, MRS Bull. **37**, 1071 (2012).

[6] M. Hinterstein, K. A. Schoenau, J. Kling, H. Fuess, M. Knapp, H. Kungl, and M. J. Hoffmann, J. Appl. Phys. **108**, 24110 (2010).

[7] B. Noheda, D. E. Cox, G. Shirane, J. A. Gonzalo, L. E. Cross, and S.-E. Park, Appl. Phys. Lett. **74**, 2059 (1999).

[8] Y. Wang, Phys. Rev. B **76**, 024108 (2007).

[9] L. A. Schmitt, K. A. Schoenau, R. Theissmann, H. Fuess, H. Kungl, and M. J. Hoffmann, J. Appl. Phys. **101**, 74107 (2007).

[10] H. Boysen, J. Phys.: Condens. Matter **19**, 275206 (2007).

[11] D. Damjanovic, Appl. Phys. Lett. **97**, 062906 (2010).

[12] H. Fu and R. Cohen, Nature (London) **403**, 281 (2000).

[13] D. Damjanovic, J. Am. Ceram. Soc. **88**, 2663 (2005).

[14] M. R. Soares, A. M. R. Senos, and P. Q. Mantas, J. Eur. Ceram. Soc. **20**, 321 (2000).

[15] M. Hinterstein, M. Hoelzel, J. Rouquette, J. Haines, J. Glaum, H. Kungl, and M. Hoffman, Acta Mater. **94**, 319 (2015).

[16] M. Hinterstein, M. Knapp, M. Hölzel, W. Jo, A. Cervellino, H. Ehrenberg, and H. Fuess, J. Appl. Crystallogr. **43**, 1314 (2010).

[17] M. Hinterstein, J. Rouquette, J. Haines, P. Papet, M. Knapp, J. Glaum, and H. Fuess, Phys. Rev. Lett. **107**, 077602 (2011).

[18] D. A. Hall, A. Steuwer, B. Cherdhirunkorn, T. Mori, and P. J. Withers, J. Appl. Phys. **96**, 4245 (2004).

[19] M. Hinterstein, L. A. Schmitt, M. Hoelzel, W. Jo, J. Rödel, H.-J. Kleebe, and M. Hoffman, Appl. Phys. Lett. **106**, 222904 (2015).

[20] M. Hinterstein, J. Rouquette, J. Haines, P. Papet, J. Glaum, M. Knapp, J. Eckert, and M. Hoffman, Phys. Rev. B **90**, 094113 (2014).

[21] N. H. Khansur, M. Hinterstein, Z. Wang, C. Groh, W. Jo, and J. E. Daniels, Appl. Phys. Lett. **107**, 242902 (2015).

[22] Z. Wang, K. G. Webber, J. M. Hudspeth, M. Hinterstein, and J. E. Daniels, Appl. Phys. Lett. **105**, 161903 (2014).

[23] M. Acosta, L. A. Schmitt, C. Cazorla, A. J. Studer, A. Zintler, J. Glaum, H.-J. Kleebe, W. Donner, M. Hoffman, J. Rödel, and M. Hinterstein, Sci. Rep. **6**, 28742 (2016).

[24] A. B. Kounga, T. Granzow, E. Aulbach, M. Hinterstein, and J. Rödel, J. Appl. Phys. **104**, 024116 (2008).

[25] H. Simons, J. E. Daniels, A. J. Studer, J. L. Jones, and M. Hoffman, J. Electroceram. **32**, 283 (2014).

[26] S. Matthies, J. Pehl, H. R. Wenk, L. Lutterotti, and S. C. Vogel, J. Appl. Crystallogr. **38**, 462 (2005).

[27] N. C. Popa and D. Balzar, J. Appl. Crystallogr. **34**, 187 (2001).

[28] D. Zhou and M. Kamlah, Acta Mater. **54**, 1389 (2006).

[29] W. Li, Z. Chen, and O. Auciello, J. Phys. D. Appl. Phys. **44**, 105404 (2011).

[30] R. Dittmer, W. Jo, E. Aulbach, T. Granzow, and J. Rödel, J. Appl. Phys. **112**, 014101 (2012).

[31] X. Chen, X. Dong, H. Zhang, F. Cao, G. Wang, Y. Gu, H. He, and Y. Liu, J. Am. Ceram. Soc. **94**, 4165 (2011).

[32] S. Zhukov, Y. A. Genenko, O. Hirsch, J. Glaum, T. Granzow, and H. von Seggern, Phys. Rev. B **82**, 014109 (2010).

[33] J. E. Daniels, C. Cozzan, S. Ukritnukun, G. Tutuncu, J. Andrieux, J. Glaum, C. Dosch, W. Jo, and J. L. Jones, J. Appl. Phys. **115**, 224104 (2014).

[34] N. Uchida and T. Ikeda, Jpn. J. Appl. Phys. **6**, 1079 (1967).

[35] J. Glaum, T. Granzow, and J. Rödel, J. Appl. Phys. **107**, 104119 (2010).